Article:
Duffy, B, Carr, HA and Möller, T (2013) Integrating isosurface statistics and histograms. IEEE Transactions on Visualization and Computer Graphics, 19 (2). 263 - 277 (14). ISSN 1077-2626

https://doi.org/10.1109/TVCG.2012.118

Integrating Isosurface Statistics and Histograms

Brian Duffy, Hamish Carr *Member, IEEE,* and Torsten Möller *Member, IEEE,*

Abstract—Many data sets are sampled on regular lattices in two, three or more dimensions, and recent work has shown that statistical properties of these data sets must take into account the continuity of the underlying physical phenomena. However, the effects of quantization on the statistics have not yet been accounted for. This paper therefore reconciles the previous papers to the underlying mathematical theory, develops a mathematical model of quantized statistics of continuous functions, and proves convergence of geometric approximations to continuous statistics for regular sampling lattices. In addition, the computational cost of various approaches is considered, and recommendations made about when to use each type of statistic.

Index Terms—histograms, frequency distribution, integration, geometric statistics

1 Introduction

MANY areas of science, engineering and medicine study continuous phenomena with scalar functions sampled finitely in two, three or more dimensions. Even where discontinuous boundaries are of interest, sampling theory still assumes that the underlying phenomena and the sampling process involve functions that are continuous everywhere or nearly everywhere. Moreover, many algorithms in visualization and analysis depend heavily on computing statistics or distributions, and these have historically been based on discrete samples rather than the underlying phenomenon.

There are three reasons why statistics in visualization must account for inter-sample continuity. First, histograms are often noisy, which impedes the ability to detect features of interest, and this is directly related to the discretization of the sampling process. Second, visualization methods such as direct volume rendering depend on continuity in order to integrate optical properties. Third, multivariate data gives multi-dimensional histograms (i.e. scatterplots) with many more bins, aggravating the problems caused by discretization. Continued improvement of visualization techniques therefore depends on a solid theoretical footing for calculating distributions from data sampled from continuous or near-continuous functions.

In this paper, we provide this theoretical footing by showing rigorously how histograms (including multi-dimensional histograms) measure geometric properties, and how to compute better approximations efficiently.

In practice, this starts with the recognition that statistics of sampled continuous functions are dependent on discretization in both domain and range. Range discretization (quantization) means that level sets are interval volumes (Section 5), while domain discretization (sampling) means that histograms approximate quantized interval volumes (Section 5). These effects can be dealt with by applying Geometric Measure Theory to integrate over the quantized interval volumes (Section 4). The principal contributions of this paper are thus:

1) We show the importance of understanding Lebesgue integration and Federer's Co-Area formula in relation to quantized data. However, while Lebesgue integration is necessary to understand the mathematical foundations of histograms, Riemann integration suffices for our proofs (Section 4).
2) We introduce the necessary correction for quantized statistics and demonstrate they are in fact *volume statistics* computed by Riemann integration (Section 6).
3) We provide a formal proof of convergence for quantized statistics and geometric properties based on Riemann integration (Section 6).

We contribute further by splitting scalar field statistics into two groups, *volume statistics* (Sections 5 and 6) and *surface statistics* (Section 7). We then show the difference between these (Section 9) and summarise which statistic to use (Section 11) based on computational performance (Section 10).

We therefore start by reviewing previous work (Section 2) and the mathematical notation (Section 3) necessary for Federer's Co-Area formula (Section 4). Supplementary materials relating to Section 4 are in Appendix I and II. Finally, Appendix III gives a detailed account of all data sets and implicit functions used for evaluation throughout this work.

2 Related Work

At the heart of this work is the relationship between histograms and other distribution statistics, geometric properties of isocontours, considerations of algorithmic efficiency, and measure theory. We will discuss measure theory in the next section and review work in visualization on statistics, geometric properties, and algorithmic efficiency in this section.

Statistical analysis of scalar fields is used in visualization for purposes such as feature detection in large volumetric data sets. Traditionally, statistical methods such as histograms are used to approximate probability distributions of scalar field data. Initially, statistical moments of distributions were

- *B. Duffy is with the Oxford Centre for Collaborative Applied Mathematics (OCCAM) at the Mathematical Institute at the University of Oxford*
- *H. Carr is with the Visualization & Virtual Reality Group at the School of Computing at the University of Leeds*
- *T. Möller is with the Graphics, Usability, and Visualization (GrUVi) Lab at the School of Computing Science at Simon Fraser University*

extracted, corresponding to statistically significant features. Other statistical moments, such as variance and standard deviation, skewness and kurtosis proposed by Tenginakai et al. [1], [2], have also been used to detect salient features.

Histograms are used in transfer function design [3] to assign optical properties to isovalues. Multidimensional histograms have been used by Kindlmann et al. [4], [5], [6] and by Kniss et al. [7], [8] to exploit relationships between isovalues and gradients. In a further variation, local histograms were proposed by Lundström et al. [9] to allow users to examine sub-regions of the volume in greater detail.

Geometric properties of isosurfaces were introduced by Bajaj et al. [10], [11] instead of histograms in visual interfaces.

Algorithmically, Shen, Hanson & Livnat [12] used the range of isovalues in each cell (the span) in data structures to accelerate isosurface extraction. Similarly, Fujishiro & Takeshima [13] extended a measure of spatial coherence from grey-scale images in 2D to volumetric data in 3D, using the difference between adjacent samples to measure coherence, and one of the principal purposes of this work was to improve the algorithmic performance of visualization techniques.

Carr et al. [14] identified the fundamental relationships between statistics, geometry and algorithmic performance, introduced continuity, and argued that algorithmic properties such as active cell count could substitute for histograms.

Scheidegger et al. [15] corrected errors in detail of this work and showed that geometric surface statistics do not measure the same properties as the histogram. They adjusted the geometric surface statistics via Federer's Co-Area formula to account for gradient changes over the scalar field, approximating the gradient with the span of the isosurfacing cells. Although based on geometric measure theory, this work approximated measures with discrete computations and overlooked the existence and contribution of cells with no span (i.e. zero gradient).

Bachthaler& Weiskopf [16] extended the continuous models to multidimensional histograms, markedly improving scatterplots for meshes representing continuous phenomena.

In summary, work in this area has unified the roles of statistics, geometry, algorithmic performance and measure theory, but left several elements unresolved: quantization in the range, the impact of cells with zero span or gradient, and whether algorithmic approximations can be guaranteed to give the same answer as the histograms. We therefore first develop some notation and summarize the relevant mathematics.

3 Definitions & Notation

Since the proofs that follow use formal definitions of integration, we state the relevant terms here, referring readers to Federer [17] or Morgan [18] for further information. We shall stick as strictly as possible to Federer's notation, although there are respects in which it could be simplified.

We also note that the geometric measure theory is not restricted to functions with one-dimensional domains and ranges, but applies more generally to functions with arbitrary dimensionality. We therefore start by assuming that we have a function $f : A \subset X = I\!R^m \to B \subset Y = I\!R^n$ from a subset A in the domain $X = I\!R^m$ to a subset B in the range $Y = I\!R^n$.

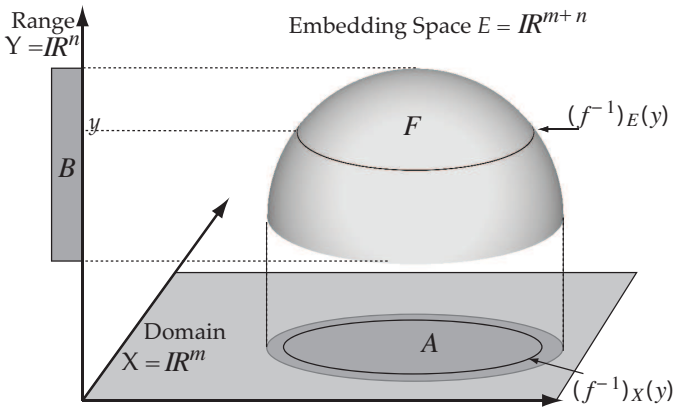

Fig. 1: Here we show the relationship between the domain $X = I\!R^m$, the range $Y = I\!R^n$, and the embedding space $E = I\!R^{m+n}$. Note how the inverse image $f^{-1}(y)$ can exist either as a subset $(f^{-1})_E(y)$ of $F \subset E$ or a subset $(f^{-1})_X(y)$ of $A \subset X$.

For convenience, we shall assume that A is of size 1 - more precisely, of m-dimensional Hausdorff measure 1 (see below).

Lipschitz Function: As defined in Federer [17], Lipschitz functions generalize the idea of functions of limited gradient - i.e. continuous functions. Thus, a function $f : X \to Y$ is a Lipschitz function from a metric space X to another metric space Y iff $\forall a,b \in A$ there is some finite number K such that:

$$d_Y(f(a), f(b)) \leq K d_X(a,b) \tag{1}$$

where d_X and d_Y are the metrics for X and Y respectively. Although this definition applies to a variety of metric spaces, we are primarily interested in Euclidean spaces, and will therefore assume that d_X and d_Y are Euclidean metrics and that the function f is Lipschitz.

Functions as Manifolds: For a Lipschitz function $f : A \subset X \to B \subset Y$, we can think of f as defining a set $F = \{(x_1,\ldots,x_m,y_1,\ldots,y_n) \in E : (x_1,\ldots,x_m) \in A, f(x_1,\ldots,x_m) = (y_1,\ldots,y_n) \in B\}$. Since f is Lipschitz, F will be an m-manifold embedded in the $m+n$-dimensional space constructed by $E = I\!R^m \times I\!R^n$, the direct sum of the spaces $X = I\!R^m$ and $Y = I\!R^n$. For convenience, we will refer to this space as the *embedding space* E of X and Y. Where $m = 2$ and $n = 1$, then $X = I\!R^2$ is the infinite plane shown in Figure 1, A is a region on the plane, and $f : A \to B$ is a height function defined on A, where $B \subset I\!R$ is the range of height values taken on by f. Moreover, the embedding space $E = A \times B \subset I\!R^2 \times I\!R^1 = I\!R^3$ is a three-dimensional space in which the function defines a terrain, and F is the terrain itself, embedded in E.

If we then project F perpendicular to $X = I\!R^m$, it projects onto A, but if we project F perpendicular to $Y = I\!R^n$, the projection of F must be B. For any given $y \in B$, we can then define the inverse image $f^{-1}(y) = \{x \in A : f(x) = y\}$, i.e. a level set in the domain A. However, we can see from the figure that it is also meaningful to discuss the inverse image as a subset of F: $f^{-1}(y) = \{(x,y) \in E : x \in A, y \in B, f(x) = y\}$. To avoid confusion, we will use $f_X^{-1}(y)$ to refer to the inverse image in A, but $f_E^{-1}(y)$ to refer to the inverse image in the embedding space. Thus, while our immediate interest involves scalar fields, the analysis also applies to multi-variate fields of the form $f : X \to Y$, as shown by Bachthaler & Weiskopf [16].

Riemann Integration: In real analysis, Riemann integration is the most commonly used form. To approximate area under a curve, the x-axis (the domain) is divided into segments. Rectangles are constructed on each segment to fit under (or over) the curve, and the area approximated as the sum of the areas of the rectangles. As the segment length approaches zero, the sum approaches the area under the curve: from below if rectangles are fitted under the curve, the lower bound, from above if rectangles are fitted over the curve, the upper bound.

This approach to integration uses Euclidean cross products between segments in the domain and range of the function to construct measuring patches, i.e. for $f : I\!R^1 \to I\!R^1$ the corresponding patch is of dimension $I\!R^1 \times I\!R^1 = I\!R^2$, a rectangle. Higher dimensional integration can be performed using the same principles by taking rectangular segments in the domain and range, where a rectangle is understood to mean a Euclidean cross product of arbitrary dimensions.

For m-dimensional domains and n-dimensional ranges, m-dimensional patches are used instead of segments, and $m+n$-dimensional regions instead of rectangles. We write:

$$\int_A f(x) d^m x \tag{2}$$

where the exponent m can be added when integrating over more than one dimension. While sufficient for most problems, Riemann integration breaks down for certain functions that are well-behaved in the range but not in the domain.

Squeeze Theorem: For a given function $f(x)$, convergence is shown by trapping $f(x)$ between upper and lower bounding Riemann integrable functions $g(x) \le f(x) \le h(x)$ for all x in an open interval containing a, except possibly $x = a$. If $\lim_{x\to a} g(x) = \lim_{x\to a} h(x) = L$, then the Squeeze Theorem forces $\lim_{x\to a} f(x) = L$, and similarly for left and right limits. We note that this is a sufficient condition for convergence of Riemann integrals: as we are using it to prove our result, we do not require it to be a necessary condition.

Lebesgue Measure: To remedy the flaws in Riemann integration, Lebesgue stepped back from integrating functions, and started with the simpler problem of measuring the size of the set B. Instead of a limit as patch size approached zero, Lebesgue used *Borel sets*: collections of subsets of A which are closed under countable union or intersection. Provided that a Borel set covers the set of interest, the Lebesgue measure $\mathscr{L}(A)$ of A replaces the concept of the limit by taking the minimum sum of sizes of Borel sets that covers A.

Lebesgue Integration: To integrate a Lipschitz function $f(x)$ over A, Lebesgue integration computes the minimal sum of sizes of the Borel elements multiplied by the value of $f(x)$ at the centre of the Borel element. When Lebesgue integration is explicitly intended, it is written as:

$$\int_A f(x) d\mathscr{L}^m x \tag{3}$$

Lebesgue measures and integration are a key aspect of geometric measure theory and are discussed in Section 4.1.

Hausdorff Measure: In general topology, sets are covered with open balls (abstractions of circles / spheres). With a similar definition to Lebesgue measures, the Hausdorff measure of an object $\mathscr{H}(A)$ is the sum of the sizes of the minimal open-ball covering of A. The Hausdorff measure is usually considered the best measure of object size, as it matches more general topological expectations. For a set of dimension m embedded in a space of dimension $m+n$, the Hausdorff measure is always m-dimensional, as it measures the intrinsic size of the set. Since we will end up with different spaces in which sets can be measured, we will make explicit the space in which we measure by writing $\mathscr{H}^m_X$ to indicate the m-dimensional Hausdorff measure in the space X.

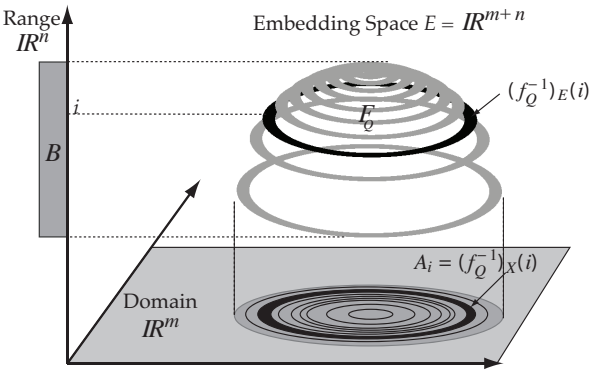

Fig. 2: Here we quantize the same function f as in Figure 1 to a function f_Q. In f_Q, only quantized values $i \in B$ have non-empty inverse images. Quantization thus replaces the manifold F with a piecewise manifold F_Q whose pieces are the inverse images $(f_Q^{-1})_E(i)$. In the domain, the corresponding inverse images become interval regions $A_i = (f_Q^{-1})_X(i)$ defined by isocontours at $i+0.5$ and $i-0.5$ of the non-quantized function.

Hausdorff Integration: We can also integrate with respect to Hausdorff measures. The process is similar to Lebesgue integration, using open balls instead of boxes, and is written:

$$\int_A f(x) d\mathscr{H}^m_X x \tag{4}$$

where the subscript indicates the space in which we measure.

Besicovich Covering Theorem: To link the Hausdorff measure to the Lebesgue measure, the Besicovich covering theorem states that measures based on patch shapes other than open balls converge provided that there is a constant ratio between the patch size and open balls.

Jacobian: A generalized version of gradient, the Jacobian is the corrective factor that relates elements of regions of the domain of a function to images of the function. For $f : I\!R^m \to I\!R^n$, differentiable at x, the Jacobian is based on the $m \times n$ differential matrix Df of the partial derivatives of each of the n output variables with respect to the m input variables.

The k-dimensional Jacobian of f, written $J_k f(x)$, is the maximum k-dimensional volume of the image under Df of a unit k-dimensional cube as described by Morgan [18]. If $rank Df(x) \le k$, then $(J_k f(x))^2$ is the sum of the squares of the determinants of the $k \times k$ submatrices of Df as per Morgan[1].

Conveniently, where $n = 1$ (i.e. f is a scalar field), the Jacobian matrix is simply an $m \times 1$ vector, and the Jacobian is the magnitude of the gradient of f, i.e. $J_1 f(x) = \|\nabla f(x)\|$. If $m = n = 1$, f is a curve embedded in two dimensions, and the

1. This definition of the Jacobian comes straight from Morgan [18] 3.6, who uses a point differentiable at a rather than x. We use x for consistency.

slope of the tangent line is the Jacobian. For arbitrary m and n, the Jacobian measures distortion from the domain A to the manifold F. For clarity, Appendix I shows a worked example.

Sampling (Discretization in the Domain): We assume that the continuous function $f : A \to B$ has been sampled at a discrete set of N distinct points P_N on a regular lattice. Since a regular lattice is defined by a set of m independent vectors $\vec{v}_j \in X = I\!R^m, j = 1 \ldots m$, each sample point p can be written as the weighted sum of integer multiples of the vectors, $p = \sum_{j=1}^{m} w_j \vec{v}_j : w_j \in \mathbb{Z}$. The set P_N of sampling points is then all distinct sample points p_i in the domain A:

$$P_N = \{p = \sum_{j=1}^{m} w_j \vec{v}_j : w_j \in \mathbb{Z}, p \in A\} \tag{5}$$

where N is determined by the number of points on the lattice within the domain A. As we will see in Section 5.3, a set of patches covering the domain is induced by the Voronoi cells of the sampling points in P_N. As N increases, these patches can then be used for Riemann integration.

Quantization (Discretization in the Range): In addition to quantizing in the domain by means of sampling, machine representations of data quantize in the range: even floating point values are quantized at the level of machine epsilon. For a scalar field $f : X \to I\!R$, the effect of this is to divide the domain into a set of disjoint regions with distinct values. In 2D, where a scalar field can be represented as a terrain in 3D, quantization results in a new function f_Q that takes the form of a set of terraces, as shown in Figure 2. Where quantization is combined with sampling, these terraces then get approximated by sets of prismatic columns perpendicular to the domain.

Level Set Measure: Given any function f, the level set measure π_f measures the size of the level set for each given value $y \in Y$. For any value of y, $\pi_f(y)$ is thus the Hausdorff measure of the inverse image $f^{-1}(y)$.

$$\pi_f(y) = \mathscr{H}^{m-n}(f^{-1}(y)) \tag{6}$$

Histogram: For a discrete set of quantized samples, the histogram is the proportion of the samples with a given value. The histogram samples are at the centers of Voronoi cells. We assume that the total volume of the domain is 1 and the size of a Voronoi cell K is $size(K) = 1/N$ (see the discussion of boundary conditions below), as there are N rectilinear Voronoi cells in each lattice, one for each sample. We therefore define the histogram over N samples to be:

$$H_N(i) = \sum_{f(p)=i, p \in P_N} size(K) \tag{7}$$

Voronoi Cells: As previously shown [14], histograms computed for a sampling involve the Voronoi cells of the samples. For each point $p \in P_N$, its Voronoi cell is the set of points that are closer to p than to any other sample:

$$Vor(p) = \{q \in A : d(q,p) < d(q,p') \forall p' \in P_N \setminus \{p\}\} \tag{8}$$

Figure 3 shows samples on a square lattice in two dimensions as dots, and their Voronoi cells as squares. Since a regular lattice uses integer-weighted sums of the basis vectors, all Voronoi cells except those at the boundaries will be homeomorphic and have the same Hausdorff measure. It is then easy to see that Nearest Neighbour interpolation reconstructs f by assigning the value $f(p)$ to each point $q \in Vor(p)$.

Delaunay Cells: Our approximations using geometric properties are not calculated with the Voronoi cells. Instead, as in Marching Cubes and related algorithms, we calculate geometric properties using the Delaunay cells $Del(P_N)$ of the point set P_N. Formally, the Delaunay complex $Del(P_N)$ is the set of cells which satisfies the condition that no point in P_N is in the interior of any closed ball circumscribing any cell in $Del(P_N)$. A point set P_N in $X = I\!R^m$ is said to be degenerate if there is any set of $m+2$ or more points from P_N on the boundary of any closed ball that contains no other vertices. If the point set is not degenerate, then all cells in $Del(P_N)$ must be simplices (triangles in 2D, tetrahedra in 3D).

Where P_N is degenerate, however, cells may be arbitrary convex polyhedra. For Cartesian sampling lattices, the Delaunay cells are m-cubes with sample points as vertices: i.e. the Delaunay cells *are* the cells used by marching algorithms.

Boundary Conditions: Voronoi cells at the boundary of the domain may not actually be homeomorphic. We avoid this by offsetting the samples by half a lattice unit, i.e. by assuming that a point sample occurs at the centre of the pixel rather than the corner. The Delaunay cells of these samples are then non-uniform, as half- and quarter- pixels occur at the boundary. To keep our computations consistent, we therefore make the simplifying assumption that the function is periodic across all boundaries, resulting in N Delaunay cells of size $1/N$ each.

4 Federer's Co-Area Formula

We now turn to one of the major results in geometric measure theory - Federer's Co-Area Formula [17]. However, the use of this work in computational statistics and visualization has varied significantly in notation, making the relationship between published papers unclear. Moreover, there is a significant flaw in how this theorem has been applied. We therefore develop the required results directly from Federer's Co-Area Formula, and use Appendix II to reconcile the notation in previous work.

4.1 Lebesgue Measures in Domain and Range

As stated above, Lebesgue integration is often used to integrate over the range of a function rather than the domain. This can be used in several ways, but the simplest is that any integral is merely the Hausdorff measure of a particular set. For example, for $f(x) : I\!R \to I\!R$, we can measure the area $\int_a^b f(x)dx$ between the curve and the x-axis, or we can measure the size of F: the arclength of a segment of f plotted in two dimensions.

For the purposes of this paper, we are primarily interested in the measure of F - but as we will see shortly, Lebesgue integration can readily be extended to other integrals. To see how various measures relate, we return to Figure 1.

Since f is a manifold F in the embedding space E, it is natural to measure A, B, or F, and to ask how these measures are related. To get the measure of A, we take:

$$\mathscr{H}_X^m(A) = \int_A 1 d\mathscr{L}^m x \tag{9}$$

For the measure of F, we start with Federer's Area Formula 3.2.3 [17], where for a Lipschitzian function $f : I\!R^m \to I\!R^{m+n}$ with $m \leq n$ and an $\mathscr{L}^m$ measurable set A:

$$\int_A J_m f(x) d\mathscr{L}^m x = \int_{I\!R^n} N(f|A,y) d\mathscr{H}^m y \quad (10)$$

Morgan [18] points out that if f is a smooth embedding, then the right hand side of Equation 10 is the Hausdorff measure of $f(A)$, i.e. the left-hand side of Equation 9. Before proceeding, we observe that Federer uses f, g, m and n to refer to different things here and in the Co-Area formula. We therefore regularize the notation by defining a mapping function $g : I\!R^m \to I\!R^{m+n} : g(x) = (x_1, \ldots, x_m, f_1(x), \ldots, f_n(x))$ which parameterizes the manifold F from the region A in the domain. Since g is Lipschitzian with $m \leq m+n$, it satisfies the requirements for Equation 10, and we can compute the Hausdorff measure of F:

$$\mathscr{H}^m_E(F) = \int_A J_m g(x) d\mathscr{L}^m x \quad (11)$$

using the Jacobian $J_m g(x)$ to correct for the projection. We give a small example in Appendix I to clarify the notation and the relationship between the Area and Co-Area Formulas.

It is also possible to compute measures of $f^{-1}(y)$ in A or in E: since y is fixed, f_E^{-1} is restricted to a subspace of E parallel to the domain X, as shown in Figure 1. The Hausdorff measure of $f^{-1}(y)$ must then be identical in X and E:

$$\begin{aligned} \pi_f(y) &= \mathscr{H}^{m-n}_X((f^{-1})_X(y)) \\ &= \mathscr{H}^{m-n}_E((f^{-1})_E(y)) \\ &= \int_{(f^{-1})_E(y)\cap F} 1 d\mathscr{H}^{m-n}_E x \end{aligned} \quad (12)$$

4.2 Federer's Co-Area Formula

For cases where Riemann integration breaks down, integration can often be done over the range $Y = I\!R^n$ rather than the domain $X = I\!R^m$. If f is invertible, this is trivial, but if not, a different approach is instead needed.

In general, f is non-invertible: $f^{-1}(y)$ is a set of dimension $m-n$ rather than a point. However, $f^{-1}(y)$ can be measured for each y, and the Co-Area formula integrates over $y \in Y$ rather than over $x \in X$. Thus, for a given $\mathscr{L}^m$ measurable set A in the domain of a Lipschitz function $f : X = I\!R^m \to Y = I\!R^n$ where $m > n$, Federer's Co-Area formula (3.2.11) states that:

$$\int_A J_n f(x) d\mathscr{L}^m x = \int_B \mathscr{H}^{m-n}(A \cap f^{-1}(y)) d\mathscr{L}^n y \quad (13)$$

Adding subscripts to show the integrating space, we get:

$$\int_A J_n f(x) d\mathscr{L}^m x = \int_B \mathscr{H}^{m-n}_A(A \cap (f^{-1})_A(y)) d\mathscr{L}^n y \quad (14)$$

In other words, we can integrate over the projection of F into the domain $X = I\!R^m$ or the projection of F into the range $Y = I\!R^n$. In either case, the integration computes the measure of patches in the projection, then multiplies those measures by a perpendicular measure estimating spatial distortion. For Riemann integration, the patches are a set of disjoint patches that sum up to either A or B, while Lebesgue integration takes the minimum sum over all Borel covers of either A or B.

Although it might seem that this equation computes the Hausdorff measure of F, the Jacobian $J_n f(x)$ used in this equation is not the same as that used in Equation 11. We provide a small example in Appendix I to clarify this issue.

Moreover, Equation 14 is primarily about measuring a region, rather than integrating a function over that region. This task of integration is done by introducing a new function in Federer's Theorem 3.2.12. In this, we take any $\mathscr{L}^m$ integrable $\overline{I\!R}$ valued function $g : X = I\!R^m \to \overline{I\!R}$ (where $\overline{I\!R}$ is the extended reals $I\!R \cup \{-\infty\} \cup \{\infty\}$). Then,

$$\int_A g(x) J_n f(x) d\mathscr{L}^m x = \int_B \int_{f^{-1}(y)} g(x) d\mathscr{H}^{m-n} x d\mathscr{L}^n y \quad (15)$$

and, with subscripts indicating the integrating space:

$$\int_A g(x) J_n f(x) d\mathscr{L}^m x = \int_B \int_{(f^{-1})_E(y)} g(x) d\mathscr{H}^{m-n}_E x d\mathscr{L}^n y \quad (16)$$

This implies several things about the use of Federer's Co-Area formula for scalar and multivariate fields and applications. We defer this discussion to Appendix II, along with the relationship between Riemann and Lebesgue integration and reconciliation of Federer's notation with that used in the related work. At this stage, we can make the following observations:

1) Although Lebesgue integration is more general than Riemann integration, many practical problems are solved with Riemann integration for the sake of simplicity.
2) Lebesgue integration was introduced in part to deal with functions that were well-behaved in the range but not in the domain. In the case of functions quantized for machine computation, we actually have functions that are well-behaved in the domain but not in the range.
3) Although Federer's Co-Area Formula uses Lebesgue-integrable functions, all of our data sets in practice are sampled at finitely many locations - our reconstructed function is therefore always Riemann-integrable.
4) For the geometric approximations of distributions introduced by Carr et al. [14], convergence is easier to prove with the mechanics of Riemann integration.

For the above reasons we will prove convergence using Riemann integration rather than Lebesgue integration.

5 Convergence of Histograms

Having understood the Co-Area Formula, we turn our attention to the histogram, and in particular, to demonstrating that the histograms of a quantized function represent volume statistics. Specifically, histograms fundamentally represent the measure of an interval volume defined by quantization.

5.1 Quantization and Interval Volumes

We consider a quantized function f_Q. In machine arithmetic, we sample with a fixed number of bits - usually 8, 12, 16 or 32. For simplicity, we assume a function f_Q that is quantized to integer values, as shown in Figure 2. Here, all function values in the range $[i-0.5, i+0.5)$ are rounded off to i, with the result that the function displays a distinct series of steps, bounded (in the domain) by the isocontours at isovalues $i-0.5$

and $i+0.5$. The inverse image of any integer $i \in B$ is then the region $A_i = f_{Q_X}^{-1}(i) \subset A$ in the domain that is bounded by these two isocontours. It then follows for scalar fields in three dimensions ($m=3, n=1$) that these regions are interval volumes, as described by Guo [19] and Fujishiro et al. [20].

5.2 Measuring the Interval Volumes

We now observe that $f_Q^{-1}(y)$ is an interval volume of dimension m iff $y \in B$ is an integer i, and of dimension 0 otherwise. It then follows that Equation 6 cannot be applied to compute an $(m-n)$-dimensional Hausdorff measure for π_{f_Q}, and that f_Q is discontinuous and thus not Lipschitz.

However, we can remedy this problem if we observe that each A_i is a bounded subset of the domain X, and that f is (still) a Lipschitz function. Applying Equation 15 to A_i, we can compute π_{f_Q} in terms of f as follows:

$$\begin{aligned}
\pi_{f_Q}(i) &= \mathscr{H}^m(A_i) \\
&= \int_{A_i} 1 d\mathscr{L}^m x \\
&= \int_Y \int_{(f^{-1})_E(y)\cap A_i} \frac{1}{\|\nabla f\|} d\mathscr{H}_E^{m-n} x d\mathscr{L}^n y \\
&= \int_{i-0.5}^{i+0.5} \int_{(f^{-1})_E(y)} \frac{1}{\|\nabla f\|} d\mathscr{H}_E^{m-n} x d\mathscr{L}^n y \quad (17)
\end{aligned}$$

Interestingly, in this form, the Jacobian is retained, and it becomes clear why the formulation in Scheidegger et al. [15] performs as desired: the Jacobian term is required for the Lebesgue integration, which is performed over an interval of size 1. Similarly, Bachthaler & Weiskopf's mass density [16] formulation already includes the Jacobian in their definition of $\sigma(\xi)$. We note that they render to an image, thus implicitly quantizing the result to bins of fixed size δy. In effect, therefore, their model performs a Riemann sum with regions of size δy, and produces the same result as the histogram.

Moreover, a corollary of this is that the sum of π_{f_Q} over all integer $i \in Y$ must be the total volume of the domain A:

$$Vol(A) = \sum_{i \in Y} \pi_{f_Q}(i) \quad (18)$$

Before covering the implications of this, we first show that the histogram converges to π_{f_Q} as sampling resolution increases.

5.3 Histogram Convergence

We take our definition of the histogram H_N, and assume that the samples are on a square lattice as in Figure 3. From Section 3, we know that the Voronoi cells in a regular square lattice are all of Hausdorff measure $size(K) = 1/N$. We claim the limit of the histogram H_N tends to π_{f_Q} as N tends to infinity:

$$\lim_{N\to\infty} H_N(i) = \pi_{f_Q}(i) \quad (19)$$

We have assumed in Section 3 that f is Riemann integrable. We therefore measure the size of the region bounded by the two contours at $i+0.5$ and $i-0.5$ using Riemann integration over the Voronoi cells of the samples, as shown in Figure 3. As the patch size approaches zero, the area computed will then converge to the correct answer in the limit. In general,

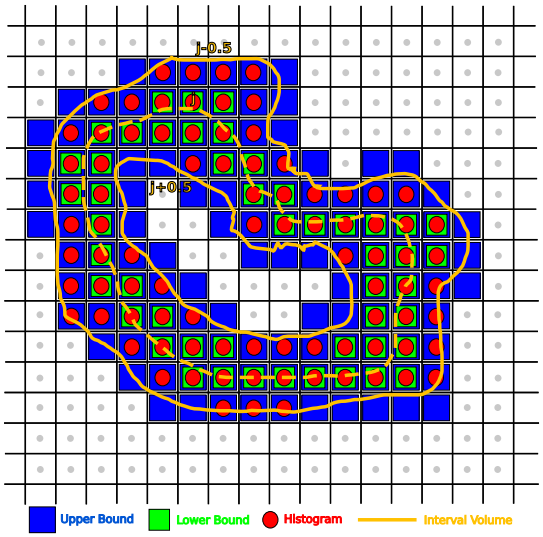

Fig. 3: The Voronoi cells of sample points can be used to prove convergence of the histogram H_N to π_{f_Q} as $N \to \infty$.

the patches need not be of uniform size, but our proofs assume a regular lattice, so all patches will be of uniform $size(K)$.

To demonstrate that the histogram converges to the measure of the interval region, we define an upper bound $U_N(i)$ and a lower bound $L_N(i)$ which are known to converge correctly by the Squeeze Theorem, and show that the histogram $H_N(i)$ is trapped between these bounds. For our lower bound $L_N(i)$, we count the set of Voronoi cells strictly contained in the interval region, as shown by green squares in Figure 3, and multiply by $size(K)$. As $L_N(i)$ is contained inside the interval region it must converge because the interval region converges. $L_N(i)$ is analogous to the lower Riemann sum of a 1D function. Similarly, for our upper bound $U_N(i)$, we choose the set of Voronoi cells intersecting the interval region, as shown as blue squares in Figure 3. As $U_N(i)$ is the total cover of the interval region it must also converge. $U_N(i)$ is analogous to the upper Riemann sum of a 1D function. By Riemann integration, these bounds converge as N increases and $size(K)$ decreases:

$$\lim_{N\to\infty} L_N(i) = \pi_{f_Q}(i) = \lim_{N\to\infty} U_N(i) \quad (20)$$

Now, as shown by red circles in Figure 3, the histogram counts all samples whose values quantize to i, i.e. all samples in the interval region A_i. We claim that $H_N(i) \geq L_N(i)$ for all N. First, every Voronoi cell in Figure 3 which is counted for $L_N(i)$ is entirely contained in A_i, and therefore the sample that defines it must be in A_i, i.e. the sample quantizes to i. It then follows that the samples corresponding to these Voronoi cells are a subset of the samples counted by the histogram, and the inequality holds. By a similar argument, $H_N(i) \leq U_N(i)$, i.e.:

$$L_N(i) \leq H_N(i) \leq U_N(i) \quad (21)$$

Then, as the Voronoi cell $size(K)$ approaches zero, the histogram is trapped between two converging sequences, and must also converge to $\pi_{f_Q}(i)$, as in Equation 19.

6 Geometric Volume Statistics

Having proven that the histogram converges to the Hausdorff measure of interval volumes, we next wish to prove that

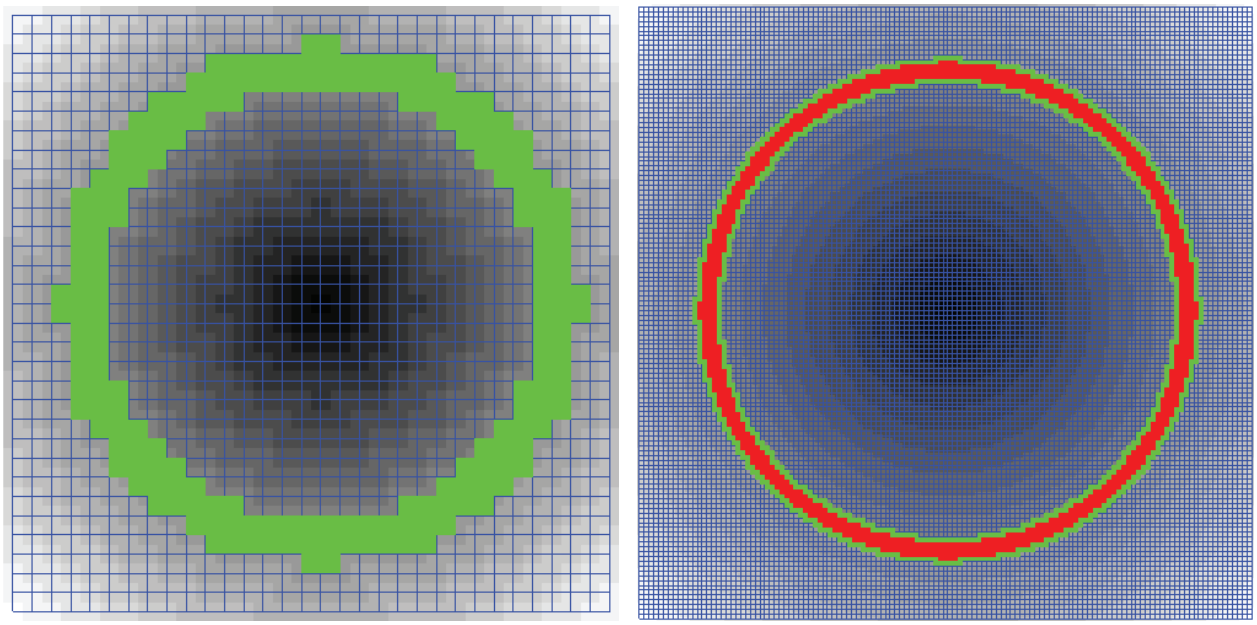

(a) 32 × 32 (b) 128 × 128

Fig. 4: In (a) and (b), a spherical distance field was sampled and quantized to the range [0-20]. Cells containing isocontour $j = 11$ are marked in green. Cells marked red are homogeneous cells, introduced by quantization, where all values equal j.

geometric approximations of volume statistics converge to the same result. However, in constructing the proof, it becomes apparent that the formulas reported by Carr et al. [14] and Scheidegger et al. [15] need correction, as they do not handle all of the consequences of quantization correctly.

Scheidegger et al. [15] approximated contour size by inverse gradient weighting either the area of triangulated isosurfaces or the number of active cells for any given isovalue, then approximated gradient magnitude with the span of the cell. While the result converged empirically, there is a subtle effect that is evident in particular for active cell count statistics.

We observe that contours are typically extracted using marching algorithms that divide the space into a mesh whose vertices are sample points, then extracted separately in each cell of the mesh. Carr et al. [14] showed that for a regular lattice of sample points, the appropriate mesh is the Delaunay complex of the samples, instead of the Voronoi complex.

For a given isovalue i, the values at a cell's vertices are compared to i and classified as *black* if their value is $> i$, *white* if $\leq i$. A surface is constructed in the cell iff some vertices are black and others white. Now consider a cubic Delaunay cell K, all of whose vertices have isovalue h. For all isovalues $< h$, all vertices are classified black, so no contour is drawn, while for isovalues $> h$, all vertices are classified white, and no contour is drawn. Under trilinear interpolation, however, every point x in the cell has function value $f(x) = h$. Correspondingly, the inverse image $f^{-1}(h) = K$ is a volume, not a surface. In practice, this is avoided by classifying vertices as white if they are $\leq i$, so no surface at all is extracted.

We refer to cells whose vertices share an isovalue as *homogeneous cells*. Since the span of such a cell is zero, using it to approximate inverse gradient magnitude would cause an exception. But contouring algorithms treat homogeneous cells as inactive for all isovalues, so no surface is extracted, and no statistic exists to be inverse gradient-weighted. As a result, Carr et al. [14] and Scheidegger et al. [15] do not process homogeneous cells, and therefore do not include them in the overall statistics - contrary to Equation 18.

TABLE 1: Empirical results from the 94 8-bit and 23 12-bit data sets used by Carr et al. [14] show a large percentage of zero spans. For the 12-bit data sets, with more quantization levels, the proportion of zero spans unsurprisingly decreases.

Type	All	Medical	Measured	Synthetic
8-bit	31.40%	25.70%	44.10%	25.20%
12-bit	8.98%	5.57%	14.72%	4.63%

6.1 Evidence of Homogeneous Cells

The existence of homogeneous cells may seem a quibble. In quantized data, however, they are surprisingly common, and affect the accuracy of geometric statistics. Before proceeding, we therefore confirm their existence in implicit functions and in real-world data. A more detailed account of these data sets can be found in Appendix III. We illustrate this in Figure 4, using a circular distance field over the domain IR^2 constrained to the sampling window $x = [-1,+1]$ and $y = [-1,+1]$. The results of this are shown in Figure 4 for the range $[0,20]$. As cell size decreases, a smaller proportion intersects the contour at isovalue $j = 11$ (shown in green), and homogeneous cells appear between active cells, as shown in red.

Once we have shown that this effect occurs for simple analytical functions, it is natural to ask whether homogeneous cells exist in real data sets. To consider this, we took the same 94 8-bit and 23 12-bit data sets used by Carr et al. [14] and computed the number of homogeneous cells in each. Table 1 reports our results - as we can see, even for scanned data sets, it is not uncommon to have $25-30\%$ of the cells homogeneous.

In practice, floating point data is re-quantized to lower precision to compute histograms of scalar fields. For this reason we restrict ourselves to the typical quantization levels 8, 10 or 12 bit. We note that for floating point data homogeneous cells will occur with much lower frequency.

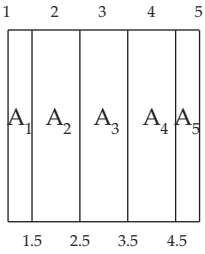

Fig. 5: Interval regions A_i intersecting a single cell K. The isovalue range in the cell is from 1.0 to 5.0, and we accordingly divide it into slabs for which f rounds off to integer values. Given linear interpolation, the slabs A_1 and A_5 are then half the width of the remaining slabs, as half of the ranges that round off to 1 and 5 are outside the cell.

We also observe that the volumetric coherence introduced by Fujishiro & Takeshima [13] relates to the homogeneous cells. These cells have zero span, and must necessarily have the same isovalue at all of the vertices. Since this implies that there are samples at isovalue i adjacent to other samples at isovalue i, homogeneous cells occur along the main diagonal of the co-occurence matrix P_δ, but are excluded from the volumetric coherence VCM by a term $(i-i)$. Since low values of VCM are taken to mean highly coherent volumes which can be rendered efficiently, the connection between statistics, geometry and algorithmic performance can again be seen.

6.2 The Histogram & Geometric Statistics

We now know that histograms approximate measures of interval volumes, and previous computations based on continuous formulas combined with discrete extraction using Marching Cubes do not correctly account for the entire domain. We will see in Section 9 the practical implications of this. First, however, we modify the formulas explicitly to account for the entire domain, and prove convergence to the correct result.

We observe that an interval region A_i includes isovalues in the range $[i-0.5, i+0.5)$. From Section 3, we assume that the Delaunay cells wrap around, and that $size(K) = Vol(A)/N$.

The span of a cell K is $span(K) = \max(K) - \min(K)$, and K intersects $span(K)+1$ interval regions A_i, as shown in Figure 5, where $span(K) = 5-1 = 4$, but there are 5 interval regions $A_1, \ldots, A_5$ intersecting the cell. Of these, A_1 covers isovalues in the range $[1.0, 1.5)$ – i.e. the range is half as great as for A_2, so we give A_1 and A_5 (i.e. $A_{\min}$ and $A_{\max}$) half as much size as the remaining regions. This is precise for linear interpolation, but not for other interpolants.

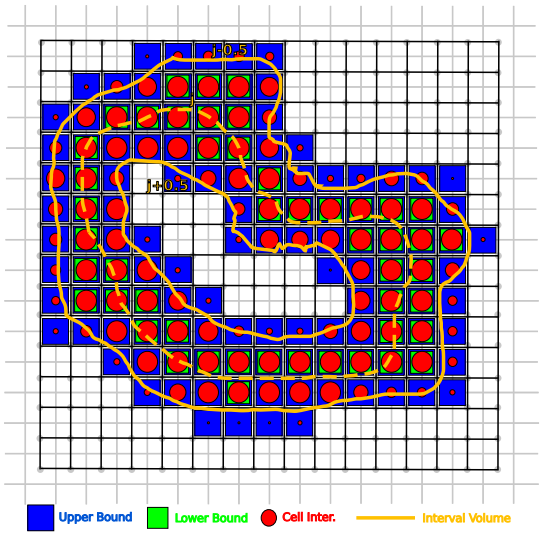

Fig. 6: For our approximations $D_N(i)$ and $C_N(i)$, the Delaunay cells of the sample points are used to prove convergence to π_{f_Q} as $N \to \infty$.

This leads to the following approximation of π_{f_Q}:

$$D_N(i) = \sum_{K \in Del(P_N)} size(K) d_i(K) \tag{22}$$

$$d_i(K) = \begin{cases} 0, & A_i \bigcap K = \emptyset \\ 1, & A_i \bigcap K \neq \emptyset, span(K) = 0 \\ \frac{1}{2span(K)}, & A_i \bigcap K \neq \emptyset, i = \min(K) \\ \frac{1}{2span(K)}, & A_i \bigcap K \neq \emptyset, i = \max(K) \\ \frac{1}{span(K)}, & otherwise \end{cases} \tag{23}$$

where $Del(P_N)$ is the Delaunay complex of P_N and $\min(K)$ and $\max(K)$ are the extremal values of the cell.

In this formulation, Delaunay cells entirely outside the interval region A_i contribute 0, those entirely inside (i.e. homogeneous cells) contribute 1, and other cells contribute a proportion of the cell based on $1/span(K)$ as shown in Figure 5. We note that the result of this is that each cell K is guaranteed to contribute 1 to the overall computation, thus preserving the measure of A as the sum of the measures of A_i:

$$Vol(A) = \sum_{i \in Y} D_N(i) \tag{24}$$

as required by Equation 18. We claim that the limit of D_N must tend to π_{f_Q} as N tends to infinity:

$$\lim_{N \to \infty} D_N(i) = \pi_{f_Q}(i) \tag{25}$$

Figure 6 shows the proof: note the parallel with the proof for the histogram, except here the integration patches are Delaunay cells instead of Voronoi cells. Delaunay cells wholly in the interval region A_i, i.e. with span zero, form the lower bound $\mathscr{L}_N(i)$ of the squeeze, while the cells that intersect the interval region A_i form the upper bound $\mathscr{U}_N(i)$. D_N is then trapped between $\mathscr{L}_N$ and $\mathscr{U}_N$ as shown in Figure 6 by shading the fraction of the cell attributed to $D_N(i)$ by Equation 23.

$$\mathscr{L}_N(i) \leq D_N(i) \leq \mathscr{U}_N(i) \tag{26}$$

Applying the squeeze principle again it follows that D_N must converge to π_{f_Q} as in Equation 25 and the result follows.

6.3 Weighted Area Convergence

As discussed in the previous work [14], [15], it is also possible to approximate the distribution function by taking the area of the isosurface for each cell and multiplying it by the inverse gradient magnitude or cell span. In effect, this replaces the isosurface with a thin shell of non-uniform thickness, that measures the volume (i.e. region size) of this shell.

This approximation also needs to be adjusted to include homogeneous cells, and proven to converge to Equation 17. As it is based on the size of the interval region A_i surrounding the contour at isovalue i, we use $C_N(i)$:

$$C_N(i) = \sum_{K \in Del(P_N)} c_i(K) \tag{27}$$

$$c_i(K) = \begin{cases} 0, & A_i \bigcap K = \emptyset \\ size(K) & A_i \bigcap K \neq \emptyset, \\ & span(K) = 0 \\ \frac{Z(K,i-0.5)}{2} \frac{t}{span(K)} & A_i \bigcap K \neq \emptyset, \\ & i = max(K) \\ \frac{Z(K,i+0.5)}{2} \frac{t}{span(K)} & A_i \bigcap K \neq \emptyset, \\ & i = min(K) \\ \frac{Z(K,i-0.5)+Z(K,i+0.5)}{2} \frac{t}{span(K)} & otherwise \end{cases} \tag{28}$$

Here, $Z(K,x)$ is the Hausdorff measure of the contour of f at isovalue x in cell K, approximated by marching cells. $t = (size(K))^{1/m}$ is a term that approximates the thickness of the cell with its linear dimension. The effect of this is to compute an approximation of the portion of $K \bigcap f_Q^{-1}(i)$. Unlike Equation 23, however, the sum of these terms is not guaranteed to sum to 1.

As with $D_N(i)$ the proof utilizes the squeeze principle, based on the recognition that we are computing region size. However, rather than treating the inverse gradient magnitude term as a fraction of the cell, we now treat it as the thickness of a shell.

We again use homogeneous cells in A_i for the lower bound $\mathscr{L}_N(i)$. We then define an upper bound for some constant k:

$$\mathscr{U}_N^k(i) = \mathscr{L}_N(i) + k(\mathscr{U}_N(i) - \mathscr{L}_N(i)) \tag{29}$$

We know that, in general, for any fixed k, f and $f+g$ converge iff f and $f+kg$ converge. Since we have shown that $\mathscr{U}_N(i)$ and $\mathscr{L}_N(i)$ converge to Equation 17. We therefore conclude that $\mathscr{U}_N^k(i)$ will also converge to Equation 17 for any fixed k. We use this conservative upper bound to simplify the proof.

As before, it is easy to see that $\mathscr{L}_N(i)$ counts exactly those homogeneous cells captured by the second branch of Equation 28, and it follows that $\mathscr{L}_N(i) \leq C_N(i)$. Now, to construct our upper bound $\mathscr{U}_N^k(i)$, we start by observing that $D_N(i)$ counted the size not only of the homogeneous cells, but also some fraction of the size of all cells on the boundary. Note that this fraction was an approximation of the portion of the cell covered by the interval region, and was computed by assuming that all interval regions intersecting the cell were the same size.

In the present instance, instead of arbitrarily dividing the cell into regions of equal size, we wish to approximate the size of the region by taking the inverse gradient as an estimate of the thickness of the interval region, and multiplying by an estimate of the other dimensions of the interval region: in this case an estimate of the length of the contour. It is not immediately clear that this approximated region will lie entirely inside the cell, and our convergence proof must adapt to this.

As the resolution gets finer, all cell dimensions get smaller: for a mesh with N cells in m dimensions, there will be $\Theta(N^{1/m})$ divisions in each dimension, and the linear dimension of each cell will scale with $(size(K))^{(1/m)}$. Moreover, for a given case in a marching cells table, since a contour fragment is $(m-1)$-dimensional, its measure will scale with $t^{m-1} = (size(K))^{\frac{m-1}{m}}$. And finally, the thickness estimated using the inverse gradient must also scale with the cell, i.e. with $t = (size(K))^{(1/m)}$.

We can now ask what the maximum region size added to $C_N(i)$ per cell is. We simplify by considering only two-dimensional square lattices, and observe that marching squares approximate a contour with line segments, and generate at most two such segments. Now, each segment lies inside a square of side t, which in turn lies inside a circumscribing circle of diameter $\sqrt{2} \cdot t$. Each of the line segments therefore has length at most $\sqrt{2} \cdot t$: since there may be at most two such line segments, $Z(K, i-0.5) \leq 2\sqrt{2} \cdot t$. Moreover, $span(K) \geq 1$, so the three lower cases of Equation 28 can contribute at most $2\sqrt{2} \cdot t \times t/1 = 2\sqrt{2} \cdot t^2 = 2\sqrt{2}(size(K))$ to the computation.

Since for each cell K intersected by the interval region, we add at most $2\sqrt{2}$ of its area to D_N, we can choose a constant $k > 2\sqrt{2}$ so that $\mathscr{L}_N$ and $\mathscr{U}_N^k$ force convergence of C_N. Note that this proof relies on a looser convergence than D_N, even though it attempts to be more accurate. We will see later that this is actually matched by looser empirical convergence.

7 Geometric Surface Statistics

In the previous sections, we showed that the histogram converges to the Hausdorff measure of interval volumes - i.e. that it is a *volume statistic*. We also showed that the formulas in Scheidegger et al. [15] converge to the same property once they have been corrected for the presence of homogeneous cells. We can now ask: if the statistics computed by Carr et al. [14] are not volume statistics, what are they?

The statistics in question were active cell counts, triangle counts and isosurface area as approximated using Marching Cubes. While the latter two are logically related to the area of an isosurface, and the data plotted by Carr et al. clearly show convergence, it is less clear why active cell counts converge to the same result, and the discovery of the role of homogeneous cells should make us suspicious of any demonstration not founded on the underlying measure theory.

We shall therefore demonstrate that all three statistics are in fact *surface statistics* - measures of particular (iso-)surfaces. In addition to this we must address the relationship of geometric surface statistics to isosurface complexity measures.

7.1 Active Cell Counts

Active cell counts are the easiest to compute, but the hardest to link logically to surface area. Paradoxically, however, they are also the easiest for which to prove convergence. We start with the Lebesgue integral: the lower bound of the size of the

Borel sets covering the region. For the Hausdorff measure, the Borel sets are spheres in the full dimension of the embedding space, rather than the intrinsic dimension of the region. Thus, the Hausdorff measure of an isosurface (a surface) is computed with a Borel set composed of spheres (volumes).

Moreover, the Besicovich Covering Theorem allows the use of any other primitive of full dimension, albeit with slower convergence. Here, we observe that, as the resolution is increased, the active cells at different resolutions form a Borel cover composed of m-cubes. The result then follows.

7.2 Triangle Counts

With this in hand, we now consider triangle counts. Empirically, Carr et al. [14] showed that these converge to the same result as the active cell count, once normalized. Since Carr, Theußl and Möller [21] showed that each cell has a reasonably reliable average number of triangles, this is hardly surprising.

Proving that triangle counts converge, however, is not easy. Each active cell will have between one and six triangles using the standard Marching Cubes cases. This was used in Section 6.3 as part of the convergence proof for weighted isosurface area. That proof, however, related to volume statistics for which the homogeneous cells dominate at higher resolutions. Thus, the contribution of the boundary cells (i.e. active cells at $i \pm 0.5$) becomes progressively smaller, and the squeeze principle can be used to establish convergence. In the case of triangle counts, the homogeneous cells are not involved, so looseness in approximation at the boundary is problematic.

In practice, therefore, we do not recommend using triangle counts for statistical purposes, as they are not proven to converge, do not empirically converge any faster than active cell counts, and are more expensive to compute.

7.3 Isosurface Area Computation

Finally, surface statistics can be approximated by explicit isosurface extraction and computation of each triangle's area. Empirically, these converge to the same result as active cell counts, which we have just proven to converge to the Hausdorff area of the isosurface. However, like triangle counts, proving convergence is difficult for the same reasons - while upper and lower bounds for each cell can be constructed, these loose bounds are not guaranteed to converge.

Thus, while isosurface area computation seems ideal, the lack of a formal proof of correct convergence should be kept in mind. Moreover, the additional computational cost means that active cell counts should be preferred in practice.

8 Isosurface Complexity

In the previous section we reviewed geometric surface statistics. Recently, surface statistics have been used to measures *isosurface complexity*, which has two meanings. The first meaning is topological complexity, such as genus, shape, smoothness and curvature of isosurfaces as described by van Gelder & Wilhelms [24]. The second meaning is algorithmic complexity, the rate of growth of the size of the isosurface k as a function of the lattice size N. More recently in the visualization literature the term *isosurface complexity* has been used to describe the latter. Isosurface complexity is a concern in visualization applications, such as isosurface extraction (Marching Cubes [25], [26]), when processing large data sets.

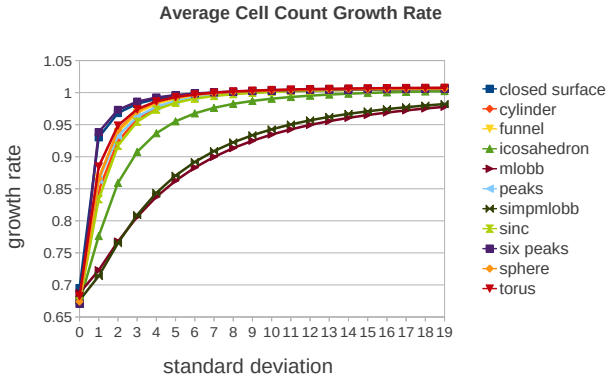

Fig. 7: Plot of noise level versus cell count for eleven implicit functions described in Appendix III. For implicit functions, noiseless volumes have average complexity close to $\Theta(N^{0.67})$, and noise moves the complexity towards the $\Theta(N)$ asymptote.

In this section we discuss how isosurface complexity relates to statistics of scalar fields and review recent results, then introduce a simple method for computing isosurface complexity based on growth rates with respect to sampling frequency.

8.1 Relation to Summary Statistics

Isosurface complexity is linked to integration and measures of surface properties. Measuring complexity adds an additional dimension to the integration, i.e. over the sampling resolution of the volume. Therefore we identify three distinct tasks that involve measuring or integrating isosurfaces.

The first task estimates *algorithmic cost* for rendering based on the geometric surface statistics in Section 7, i.e. cell and triangle counts, and should be treated as such. While this formed the original motivation of Carr et al. [14], in retrospect rendering cost is better predicted by the maximum number of triangles rather than the average as it represents the worst case for asymptotic analysis. We return to this in Section 8.3.

The second task computes a *summary statistic* for a data set, and is a volume statistic. For this, Scheidegger et al. [15] as modified in Section 6 are correct. For measuring algorithmic complexity, however, the gradient is not required.

The final task, computing *fractal complexity* of noisy data [23], computes complexity from fractal box span dimensions of a 2-manifold in a 3-space. This measures the intrinsic complexity or dimensionality of the function, and is therefore different from the previous two tasks.

8.2 Related Results

While introducing a new isosurface extraction technique, Itoh & Koyamada [22] made a passing observation that isosurfaces, being planar, should have a growth rate of $\Theta(N^{\frac{2}{3}})$ and proposed triangle counts to approximate isosurface size k. Carr et al. [14] measured isosurface growth empirically as a function of N, by counting triangles in ninety data sets and fitting a least squares line to the data. The slope of the line was used to estimate a growth rate of $\Theta(N^{0.82})$.

TABLE 2: A summary of isosurface complexity measures to date.

Year	Paper	Approximation(k)	All	Medical	Measured	Synthetic	Implicit Functions
1994	Itoh & Koyamada [22]	Triangle Count	$\Theta(N^{0.67})$	-	-	-	-
2006	Carr et al. [14]	Triangle Count	$\Theta(N^{0.82})$	$\Theta(N^{1.05})$	$\Theta(N^{0.54})$	$\Theta(N^{0.80})$	-
2008	Scheidegger et al. [15]	Weighted Isosurface Area	$\Theta(N^{0.96})$	$\Theta(N^{0.70})$	$\Theta(N^{0.87})$	$\Theta(N^{0.82})$	$\Theta(N^{0.67})$
2010	Khoury & Wenger [23]	Fractal Dimensions & Cells	$\Theta(N^{0.75})$	$\Theta(N^{0.76})$	$\Theta(N^{0.75})$	$\Theta(N^{0.73})$	-
2012	Duffy et al.	Down-sampled Triangles	$\Theta(N^{0.76})$	$\Theta(N^{0.77})$	$\Theta(N^{0.75})$	$\Theta(N^{0.77})$	$\Theta(N^{0.67})$
2012	Duffy et al.	Down-sampled Cells	$\Theta(N^{0.71})$	$\Theta(N^{0.71})$	$\Theta(N^{0.70})$	$\Theta(N^{0.71})$	$\Theta(N^{0.65})$

Scheidegger et al. [15] then argued that average isosurface complexity should account for the gradient and introduced the Co-Area formula. They used gradient weighted isosurface area to estimate k, which yielded a growth rate of $\Theta(N^{0.96})$. Scheidegger et al. [15] also showed that for clean implicit functions the growth rate is approximately $\Theta(N^{\frac{2}{3}})$, but that noise increases this. We know from Section 6 that gradient weighting gives us volume statistics: they are therefore not an appropriate measure of algorithmic complexity.

Khoury & Wenger [23] estimated a growth rate of $\Theta(N^{0.75})$ by measuring the fractal dimensions of isosurfaces using cell intersections to approximate k. They count active cells because the cell counts are independent of the specific approximation methods used in isosurface reconstruction. Furthermore, they showed the fractal dimension of an isosurface is proportional to the topological noise in the data. They measured topological noise for an isosurface by computing the number of connected components and dividing by the edge intersections to correct for the dependency on isosurface area.

8.3 Asymptotic Analysis Approach

In this section we introduce a new method for measuring isosurface complexity based on a multi-scale approach. We use multiple down-sampled versions of sixty data sets to compute the growth of k as a function of N: a method suggested but not implemented by Khoury & Wenger [23]. As the lattice density increases, we measure the active cell and triangle counts at each resolution. The growth rate for each isosurface is then found from the slope of a log-log least squares line, and shown in Table 2 and Figure 7. As we see in Table 2, these approximations are similar to the prediction by Itoh & Koyamada [22]. From the variation in results, we see that the approximation chosen for isosurface reconstruction affects the computed growth rate, as predicted by Khoury & Wenger [23].

In addition to this we compute average cell count complexity for eleven implicit functions and add synthetic Gaussian noise in Figure 7. This verifies the result of Scheidegger et al. [15] for implicit functions. Noiseless volumes have average complexity of approximately $\Theta(N^{0.67})$. Adding noise to the volume moves the complexity towards the $\Theta(N)$ asymptote. The list of data sets used can be found in Appendix III.

In practice, average complexity does not have a clear meaning. Instead, implicit functions tend to have smooth interfaces between regions in the data, so their complexity measures are not representative of real data. For real data, peaks representing significant features tend to be distributed asymmetrically with large standard deviations. Thus, while implicit functions give a lower bound, and an upper bound of $O(N)$ is provable, Khoury & Wenger [23] showed that the expectation is intermediate between these bounds and fractal in nature.

In Section 8.1 we noted that worst case performance should be used to predict *algorithmic cost*. For isosurface extraction this means taking the isosurface with the maximum growth rate. We also note that computing the average isosurface growth rate for a given data set has very little meaning for two reasons. Firstly, average isosurface growth does not reflect how the user interacts with the isosurface extraction algorithm and may not represent a statistically significant feature in the data. Secondly, averaging implies integrating over the range of the data set and may compute the growth rate of an isosurface that does not exist when dealing with quantized data.

We therefore compute the average worst and best case growth rates from a population of 60 data sets, a subset of the 77 data sets in Appendix III. Data sets with a dimension less than 64 samples were excluded to maintain sufficient sample density when down-sampling, i.e. a data set $128 \times 256 \times 32$ would be excluded. In practice, the average worst case for down-sampled cells is estimated at $\Theta(N^{0.87})$ for all real data sets, $\Theta(N^{0.89})$ for medical, $\Theta(N^{0.89})$ for measured, $\Theta(N^{0.83})$ for synthetic and $\Theta(N^{0.76})$ for implicit functions. The average best case for down-sampled cells is estimated at $\Theta(N^{0.42})$ for all data sets $\Theta(N^{0.44})$ for medical, $\Theta(N^{0.42})$ for measured, $\Theta(N^{0.41})$ for synthetic and $\Theta(N^{0.23})$ for implicit functions.

9 Comparison with Previous Methods

In previous sections, we established that histograms and other volume statistics provably converge to the interval volume measure, that active cell counts converge to isosurface area, and that other surface statistics empirically converge to isosurface area. It remains to test whether adding homogeneous cells to the computation makes any significant difference.

We start with the Marschner-Lobb [27] dataset at 41^3 resolution. We compared the histogram with the statistics reported by Carr et al. [14], by Scheidegger et al. [15], and the updated volume statistics in Equation 22 and Equation 27. For clarity, volume statistics based on cell intersections are shown on the left of Figure 10, while those based on weighted isosurface areas are shown on the right.

In these figures we see that, as previously reported, histograms give poor approximations of interval volume measures at low resolutions, and that volume statistics give smoother estimates. Misleadingly, the active cell count reported by Carr et al. [14], shown in blue, appears to give the same distribution as the other statistics, presumably because the gradient in the Marschner-Lobb signal is fairly uniform. Moreover, although there are minor differences between the results of the formula reported by Scheidegger et al. [15] and Equation 22 and Equation 27, there is little to choose between them in practice.

At higher resolution, in Figure 9, we see that the histogram has converged to the same result as the other volume statistics, but that the simple count of intersected cells has converged to a different result. We also see that, at the margins of the distribution, Equation 22 and Equation 27 converge slightly better than the statistics from Scheidegger et al. [15].

One might conclude that there is no point to improving the computation, but this is not true, as can be seen in Figure 10,

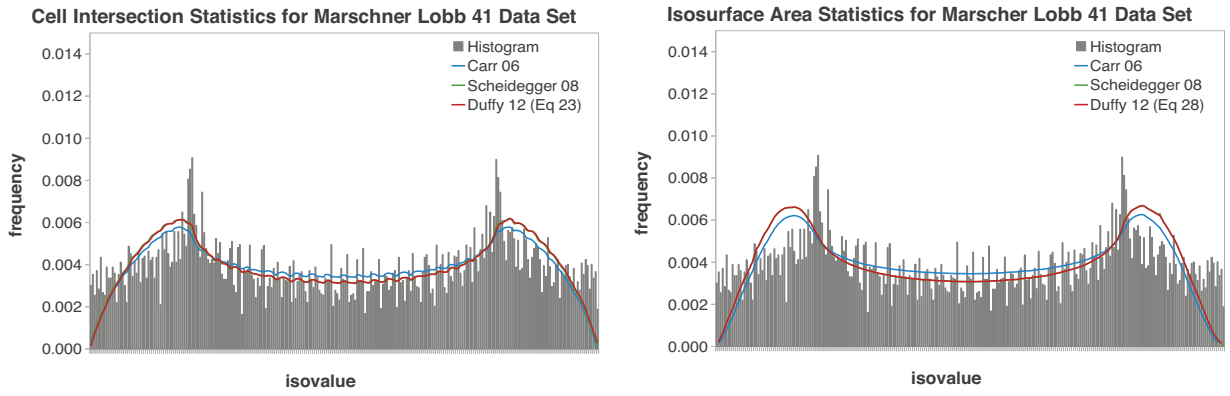

Fig. 8: Comparison of volume statistics for $41 \times 41 \times 41$ resolution sampling of the Marschner-Lobb test signal. As in previous work, it is apparent that volume statistics of low-resolution data are of better quality than histograms.

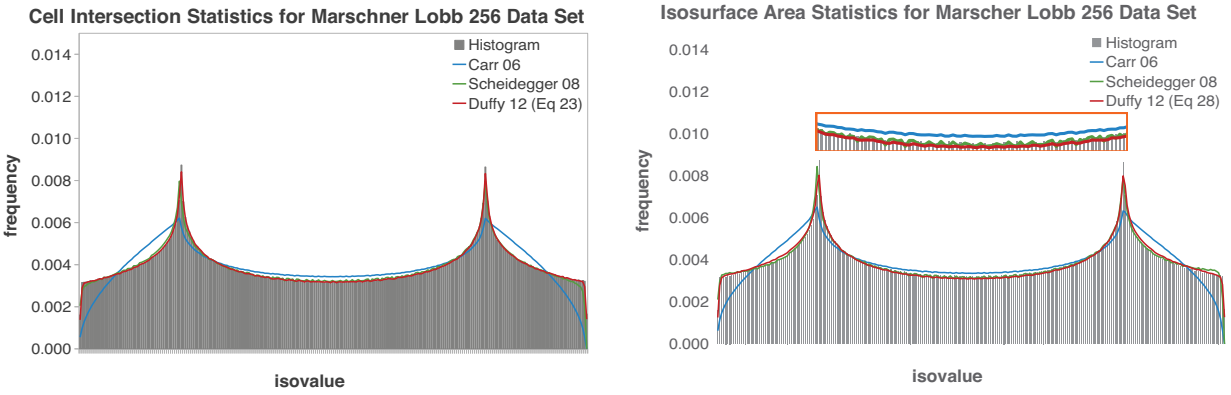

Fig. 9: Comparison of volume statistics for $256 \times 256 \times 256$ resolution sampling of the Marschner-Lobb test signal. At high resolutions, the histogram has converged reasonably well, and no advantage is seen from the use of volume statistics. Minor differences are visible when homogeneous cells are added to the computations.

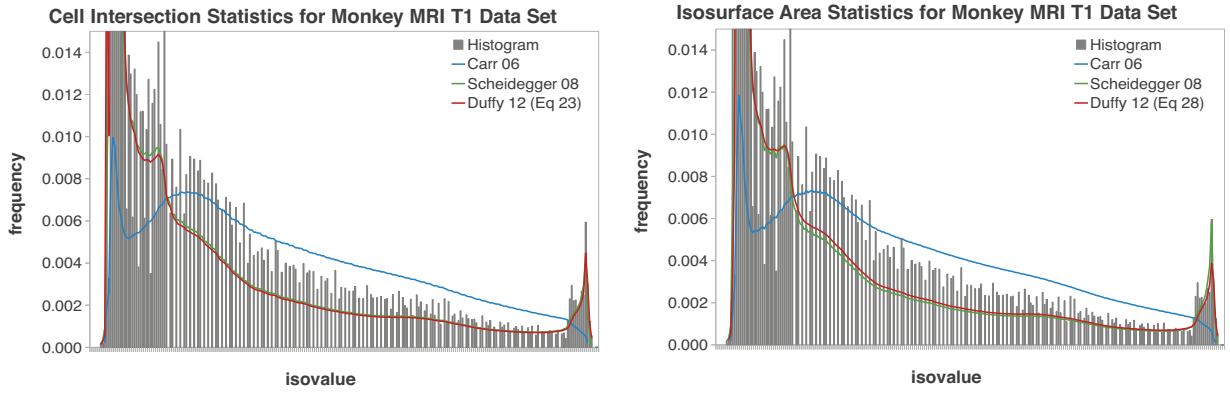

Fig. 10: Comparison of volume statistics for Monkey-MRI-T1 data. Here, the data is of very uneven quality, and the updated computation with homogeneous cells shows a marked improvement compared to previous work. Moreover, the difference between surface statistics (blue) and volume statistics becomes apparent.

an MRI scan of a monkey. Again, the simple count of intersected cells is clearly a different result from either histogram or volume statistic. Since we have already concluded above that this is actually a surface statistic, this poses no difficulty. But, when we compare the cell intersection statistics, we see that the computation in Scheidegger et al. [15] struggles with the uneven quantization of the underlying data, resulting in a sequence of cusps rather than the smoother line that results from counting homogeneous cells as well.

For high-resolution data sets, then, histograms are sufficiently high quality that no other volume statistics are merited. However, at lower resolutions, or for data with hidden

sampling issues, geometric statistics are more reliable.

10 Computational Performance

As well as the relative quality of these approaches, we can also consider the computational cost. Due to the simplicity of the computation, we would expect histograms to be cheapest. We would also expect weighted cell counts to be cheaper than weighted isosurface area, as there is no need to extract and measure triangles. The updated volume computations of Equation 22 and Equation 27 should be slightly more expensive than the weighted cell counts and weighted isosurface area from Scheidegger et al. [15], since a small amount of additional computation is required.

In Figure 11 (left), we show the computation cost in seconds of the volume statistics for the same data sets as used by Carr et al. [14], plotted against the data size. As expected, the performance advantage of the histograms shows up quite clearly, with the two weighted cell intersection computations next, and the two weighted isosurface area computations last. And, also as expected, the corrections introduced in Equation 22 and Equation 27 add little or no additional cost.

Similarly, Figure 11 (right) shows the comparative computation cost in seconds of the surface statistics originally reported by Carr et al. [14], with histograms plotted for comparison. Again, while histograms are clearly cheapest to compute (although not computing the same property), cell intersection counts are much cheaper than isosurface area computations.

TABLE 3: Computational costs of volume and surface statistics. Histograms are cheapest by at least an order of magnitude, followed by cell counting, followed by area approximations, again by an order of magnitude. As expected, the corrections introduced in Equation 22 and Equation 27 increase the cost by only a small amount.

Paper	Volume Statistics	Slope s / Msample
-	Histogram	0.0242
Scheidegger et al. [15]	Weighted Cell Intersection	0.5626
Duffy et al. Equation 23	Interval Volume Cell Count	0.5921
Scheidegger et al. [15]	Weighted Isosurface Area	6.8053
Duffy et al. Equation 28	Interval Volume Approximation	8.1168
	Surface Statistics	
Carr et al. [14]	Cell Intersection	0.5349
Carr et al. [14]	Isosurface Area	6.8387

Since these computations are all performed one voxel or one grid cube at a time, we expect them to scale linearly with the data size, and within broad terms they do. We therefore plotted least squares fitted lines for each statistic, and report summary statistics in Table 3. We can see from these statistics that histograms are cheaper by one and a half orders of magnitude than all intersection cell computations, which in turn are an order of magnitude cheaper than isosurface area computations.

11 Assessment

We have now seen that the statistics reported in previous work converge to one of two fundamental properties. Histograms and the corrected weighted cell intersection counts of Equation 22 converge to the measure of the interval volume. Cell intersection counts and isosurface area approximations converge instead to the Hausdorff measure of the isosurface area.

We have seen, however, that some statistics give smoother results than others, especially at low resolution, and that some statistics are cheaper to compute than others. Given these observations, we can now make the following recommendations:

1) For high-resolution volume statistics, histograms give sufficiently high-quality results most of the time that their speed advantage dictates their use.
2) For low-resolution volume statistics, interval volume cell counts should be used, as they balance quality and speed better than either histograms or interval volume approximations. Equation 22 should be used instead of the formula reported by Scheidegger et al [15].
3) For surface statistics, cell intersection counts should be used, as they are cheap and converge rapidly.

12 Conclusions & Future Work

We have shown that previous papers on geometric statistics of continuous functions can be reconciled to the underlying mathematical model of Federer's Geometric Measure Theory. We have also shown that histograms are statistics that approximate the volumetric measure of the interval volume defined by the quantization of data in the range, and that the same property can also be computed by approximations based either on counting cells intersecting the interval volume, or computations measuring the interval volume extracted by Marching Cubes. We have further shown that computing these approximations correctly requires accounting for homogeneous cells - cells all of whose vertex isovalues are identical.

We have also confirmed that the level set measure $\pi_f(y)$ of a function f is the Hausdorff measure of $f^{-1}(y)$ in the domain, and that this can be approximated either by isosurface area extraction and mensuration or simply by counting active cells.

Finally, we have shown that the choice of which statistic to compute can be driven by assessing the tradeoff between computational cost and quality of result.

Some future directions arise from this. First, none of the computations herein are restricted to volumetric data or to the Cartesian lattice: the proofs generalise to higher dimensions in both domain and range and to non-Cartesian lattices. Federer's Area and Co-Area formulas for Lipschitzian maps of functions only work for m-dimensional measures over subsets of n-dimensional Euclidean space, i.e. $m \leq n$. Bachthaler & Weiskopf explicitly dealt with $m = n$, and we would like to extend this work to $m > n$ and to irregularly sampled data.

We would like to consider the impact of geometric measure theory on other geometric properties such as higher-order moments and sphericity. Since these involve second and higher derivatives, we expect that the homogeneous cells will be increasingly important. In broad terms, we predict that where these properties are being used to underpin transfer function design, adjustments will be needed to base them on the interval regions rather than local properties of isosurfaces, but the details of this will take considerable effort to work out.

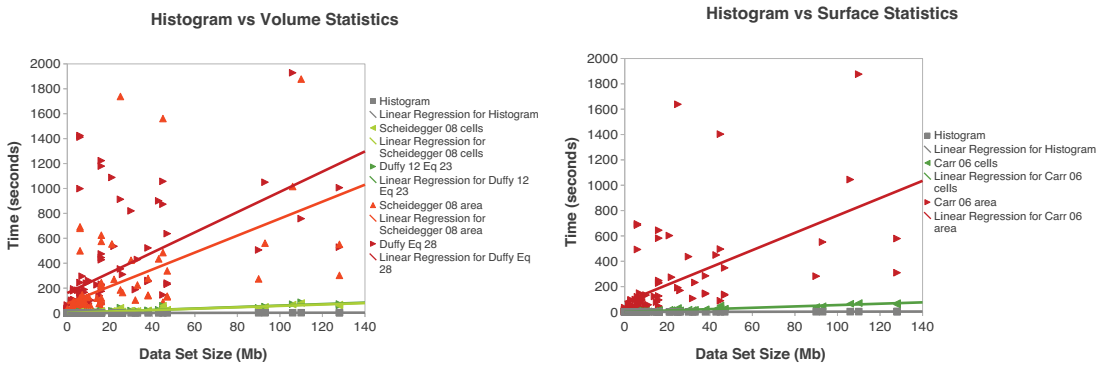

Fig. 11: Performance Characteristics of volume and surface statistics. As predicted, histograms are cheapest to compute, followed by cell counted statistics, followed by triangle-area computations.

We intend to explore the use of these statistics to assess relative convergence properties of different sampling lattices. We note that, logically, if inverse gradient-weighted cell counts approximate interval volumes as do histograms, that gradient-weighted histograms ought to approximate isosurface area computations, potentially at cheaper cost than cell counts.

Furthermore, the identification of the gradient relationship between the two types of statistics (re)-raises an interesting question: if histograms relate to inverse-gradient weighted statistics, are surface statistics such as active cell counts a better statistic for detecting high-gradient boundaries in data?

Acknowledgements

We would like to thank University College Dublin for financial support for this research, and both Barry Denby and Brian MacCarthy for their contributions to this work.

References

[1] S. Tenginakai, J. Lee, and R. Machiraju, "Salient iso-surface detection with model-independent statistical signatures," *Proceedings of IEEE Visualization*, pp. 231–238, 2001.

[2] S. Tenginakai and R. Machiraju, "Statistical computation of salient iso-values," *Proceedings of the Symposium on Data Visualisation (VisSym)*, pp. 19–24, 2002.

[3] H. Pfister, B. Lorensen, C. Bajaj, G. Kindlmann, W. Schroeder, L. S. Avila, K. Martin, R. Machiraju, and J. Lee, "The transfer function bake-off," *IEEE Computer Graphics and Applications*, vol. 21, no. 3, pp. 16–22, May 2001.

[4] G. Kindlmann and J. W. Durkin, "Semi-automatic generation of transfer functions for direct volume rendering," *Proceedings of the 1998 IEEE Symposium on Volume Visualization*, pp. 79–86, 1998.

[5] G. Kindlmann, "Semi-automatic generation of transfer functions for direct volume rendering," Master's thesis, Cornell University, 1999.

[6] G. Kindlmann, R. Whitaker, T. Tasdizen, and T. Möller, "Curvature-based transfer functions for direct volume rendering: Methods and applications," *Proceedings of IEEE Visualization 2003*, pp. 513–520, October 2003.

[7] J. Kniss, G. Kindlmann, and C. D. Hansen, "Interactive volume rendering using multi-dimensional transfer functions and direct manipulation widgets," in *Proceedings of IEEE Visualization*, 2001, pp. 255–262, 562.

[8] ——, "Multidimensional transfer functions for interactive volume rendering," *IEEE Transactions on Visualization and Computer Graphics*, vol. 8, no. 3, pp. 270–285, July 2002.

[9] C. Lundström, P. Ljung, and A. Ynnerman, "Local histograms for design of transfer functions in direct volume rendering," *IEEE Transactions on Visualization and Computer Graphics*, vol. 12, no. 6, pp. 1570–1579, 2006.

[10] C. Bajaj, V. Pascucci, and D. Schikore, "The contour spectrum," *Proceedings of IEEE Visualization*, pp. 167–173, 1997.

[11] C. L. Bajaj, V. Pascucci, and D. Schikore, "Accelerated isocontouring of scalar fields," *Data Visualization Techniques. New York: Wiley*, pp. 31–47, 1999.

[12] H.-W. Shen, C. D. Hansen, Y. Livnat, and C. R. Johnson, "Isosurfacing in Span Space with Utmost Efficiency (ISSUE)," in *Proceedings of Visualization 1996*, 1996, pp. 287–294.

[13] I. Fujishiro and Y. Takeshima, "Coherence-sensitive solid fitting," *Computers and Graphics*, vol. 26, pp. 417–427, 2002.

[14] H. Carr, B. Duffy, and B. Denby, "On histograms and isosurface statistics," *IEEE Transactions on Visualization and Computer Graphics*, vol. 12, no. 5, pp. 1259–1266, 2006.

[15] C. E. Scheidegger, J. M. Schreiner, B. Duffy, H. Carr, and C. T. Silva, "Revisiting histograms and isosurface statistics," *IEEE Transactions on Visualization and Computer Graphics*, vol. 14, no. 6, pp. 1659–1666, 2008.

[16] S. Bachthaler and D. Weiskopf, "Continuous scatterplots," *IEEE Transactions on Visualization and Computer Graphics*, vol. 14, no. 6, pp. 1428–1435, 2008.

[17] H. Federer, *Geometric Measure Theory*. Springer-Verlag, 1965.

[18] F. Morgan, *Geometric Measure Theory: A Beginner's Guide*. Academic Press, 1988.

[19] B. Guo, "Interval set: A volume rendering technique generalizing isosurface extraction," *Proceedings of IEEE Visualization*, pp. 3–10, 1995.

[20] I. Fujishiro, Y. Maeda, and H. Sato, "Interval volume: A solid fitting technique for volumetric data display and analysis," in *Proceedings IEEE Visualization*. Los Alamitos, CA, USA: IEEE Computer Society, 1995, pp. 151–158.

[21] H. Carr, T. Theußl, and T. Möller, "Isosurfaces on optimal regular samples," in *VISSYM '03: Proceedings of the Symposium on Data Visualisation 2003*. Aire-la-Ville, Switzerland, Switzerland: Eurographics Association, 2003, pp. 39–48.

[22] T. Itoh and K. Koyamada, "Isosurface generation by using extrema graphs," *in Proceedings of the IEEE Conference on Visualization*, pp. 77–83, 1994.

[23] M. Khoury and R. Wenger, "On the fractal dimension of isosurfaces," *IEEE Transactions on Visualization and Computer Graphics*, vol. 16, no. 6, pp. 1198–1205, Nov.-Dec. 2010.

[24] A. van Gelder and J. Wilhelms, "Topological considerations in isosurface generation," *ACM Transactions on Graphics*, vol. 13, pp. 337–375, 1994.

[25] W. E. Lorensen and H. E. Cline, "Marching cubes: a high resolution 3D surface construction algorithm," *in Proceedings of the SIGGRAPH Conference on Computer Graphics and Interactive Techniques*, pp. 163–169, 1987.

[26] T. S. Newman and H. Yi, "A survey of the Marching Cubes algorithm," *Computers And Graphics*, pp. 854–879, 2006.

[27] S. R. Marschner and R. J. Lobb, "An evaluation of reconstruction filters for volume rendering," *in Proceedings of the IEEE Conference on Visualization*, pp. 100–107, 1994.

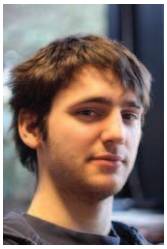

Brian Duffy Brian Duffy received a BSc in computer science from University College Dublin, Ireland in 2006. He received his PhD in visualization and computer graphics from the the same institution in 2011. He is currently working for the Oxford Centre for Computational and Applied Mathematics at the University of Oxford. His research interests include scientific visualization with application to mathematical problems.

Hamish Carr completed his PhD at the University of British Columbia in May 2004 and has worked as a lecturer at University College Dublin and a senior lecturer at the University of Leeds. His research interests include scientific and medical visualization, computational geometry and topology, computer graphics and geometric applications. He is a member of the IEEE and the IEEE Computer Society.

Torsten Möller is a professor at the School of Computing Science at Simon Fraser University. He received his PhD in Computer and Information Science from Ohio State University in 1999 and a Vordiplom (BSc) in mathematical computer science from Humboldt University of Berlin, Germany. He is a senior member of IEEE and ACM, and a member of Eurographics. His research interests include the fields of Visualization and Computer Graphics, especially the mathematical foundations thereof.

He is co-director of the Graphics, Usability and Visualization Lab (GrUVi). He is the appointed Vice Chair for Publications of the IEEE Visualization and Graphics Technical Committee (VGTC). He has served on a number of program committees and has been papers co-chair for IEEE Visualization, EuroVis, Graphics Interface, and the Workshop on Volume Graphics as well as the Visualization track of the 2007 International Symposium on Visual Computing. He has also co-organized the 2004 Workshop on Mathematical Foundations of Scientific Visualization, Computer Graphics, and Massive Data Exploration as well as the 2010 Workshop on Sampling and Reconstruction: Applications and Advances at the Banff International Research Station, Canada. He is a co-founding chair of the Symposium on Biological Data Visualization (BioVis). In 2010, he was the recipient of the NSERC DAS award.